

RESEARCH ARTICLE

10.1029/2018JB016189

Key Points:

- We present a new empirical method for InSAR tropospheric corrections using high-resolution weather model products
- A spatially varying scaling factor is used to refine the magnitude of tropospheric delays
- We improve the isolation of the deformation signal across the Altyn Tagh Fault zone, which spans 6,000 m of topographic relief

Supporting Information:

- Supporting Information S1

Correspondence to:

L. Shen,
eels@leeds.ac.uk

Citation:

Shen, L., Hooper, A., & Elliott, J. (2019). A spatially varying scaling method for InSAR tropospheric corrections using a high-resolution weather model. *Journal of Geophysical Research: Solid Earth*, 124, 4051–4068. <https://doi.org/10.1029/2018JB016189>

Received 12 JUN 2018

Accepted 12 MAR 2019

Accepted article online 14 MAR 2019

Published online 5 APR 2019

Corrected 20 MAY 2019

This article was corrected on 20 MAY 2019. See the end of the full text for details.

A Spatially Varying Scaling Method for InSAR Tropospheric Corrections Using a High-Resolution Weather Model

Lin Shen¹ , Andrew Hooper¹ , and John Elliott¹ 

¹COMET, School of Earth and Environment, University of Leeds, Leeds, UK

Abstract Variation in tropospheric delay is a major limiting factor on the accuracy of interferometric synthetic aperture radar (InSAR) measurements. This is particularly the case when deformation and topography are correlated. To address limitations of previous InSAR tropospheric correction methods, here we present a new approach that combines the use of both external weather model data and the interferometric phase. We assume that vertical refractivity profiles calculated from a high-resolution weather model data can generally describe the form of the relationship between tropospheric delay and height but that the magnitude can be incorrect. We estimate a magnitude correction by scaling the original delays to best match the interferometric phase. We validated our new method using simulated data and demonstrate that both coseismic and interseismic signals can be separated from strong tropospheric delays. We also applied our algorithm to the central portion of the Altyn Tagh Fault in northern Tibet, where deformation correlates strongly with topographic relief of 6,000 m, and show that the derived velocity field is more internally consistent and agrees better with independent Global Positioning System measurements.

1. Introduction

As a geodetic tool, Interferometric Synthetic Aperture Radar (InSAR) is used to measure ground deformation such as interseismic slip (e.g., Daout et al., 2018; Fialko, 2006; Hussain et al., 2016; Jolivet et al., 2008; Walters et al., 2013; Wei et al., 2010), earthquake deformation (e.g., Ainscoe et al., 2017; Delouis et al., 2010; Hamling et al., 2017; Lindsey et al., 2015), volcanic dike intrusions (e.g., Sigmundsson et al., 2015), landslides (e.g., Singleton et al., 2014; Yin et al., 2010), and urban subsidence (e.g., Chaussard et al., 2014; Perissin & Wang, 2011). The recently launched Sentinel-1 constellation can achieve high spatial resolution and short revisit times with a wide spatial coverage, which has improved the coherence of interferograms and so increased the potential of precise and large-scale InSAR studies of tectonic processes (Elliott et al., 2016). However, variation in the phase delay, caused by the spatiotemporal variability of tropospheric properties, is still a major limiting factor in Sentinel-1 InSAR measurements (Parker et al., 2015), particularly when deriving long wavelength deformation signals that are partially correlated with topography.

Tropospheric delays depend on temperature, pressure, and relative humidity and can be split into hydrostatic and wet components. In flat regions, hydrostatic delays are usually smooth in space as they are predominantly pressure dependent. However, in areas of significant relief, spatial variations in hydrostatic delays are strong and can lead to a correlation between phase and topography (Elliott et al., 2008). Therefore, while it has been possible to measure relatively small interseismic signals in flat regions of the Tibetan Plateau (Bell et al., 2011; Taylor & Peltzer, 2006), it has previously been hard to measure such deformation with high accuracy at the steep margins of the Plateau. In contrast to hydrostatic signals, the magnitude of wet delays, which are caused by the lateral variation in water vapor, is several times smaller (Hanssen, 2001), whereas the spatial pattern is much more variable (Zebker et al., 1997). Both the hydrostatic and wet delays should be accounted for to fully describe the tropospheric delays (Doin et al., 2009; Elliott et al., 2008; Puységur et al., 2007). Tropospheric effects can cause variations of up to 15–20 cm in magnitude over a distance on the order of 100 km, which would overwhelm most slowly accumulating deformation or time-dependent signals (Bekaert, Walters, et al., 2015; Fournier et al., 2011; Heleno et al., 2010; Hooper et al., 2012).

To reduce the tropospheric effects, various approaches have been tried, using either external data or the interferometric phase itself. External data sets that have been utilized include local meteorological data (e.g.,

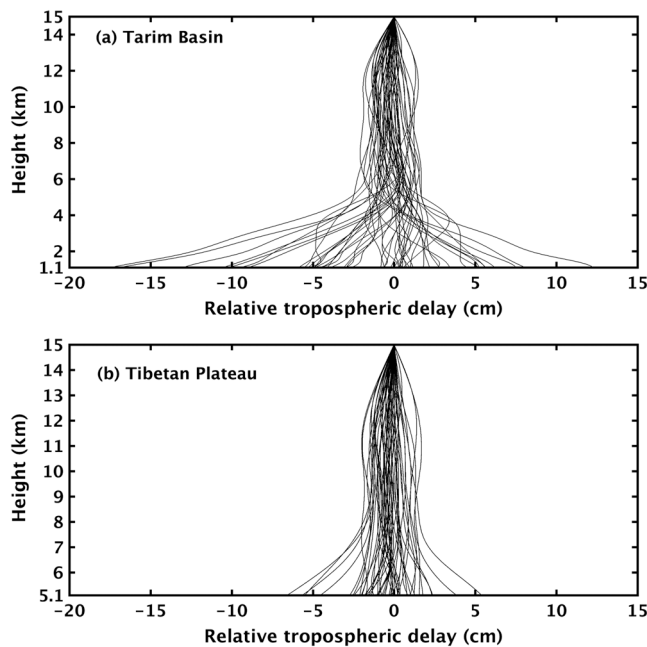


Figure 1. Relative tropospheric delays estimated from the high resolution European Centre for Medium-Range Weather Forecasts products for 53 small baseline interferograms (Figure S1) over northern Tibet. Each curve shows the relative tropospheric delays for a point in (a) the Tarim Basin (85.6°E, 38.3°N) or (b) the Tibetan Plateau (86.1°E, 36.8°N) from the surface (note difference in surface elevation of 1.1 vs. 5.1 km).

Delacourt et al., 1998; Pinel et al., 2011), continuous Global Positioning System (GPS) zenith delay measurements (e.g., Li et al., 2006; Onn & Zebker, 2006; Yu et al., 2017), spectrometer measurements (e.g., Li et al., 2009), numerical metrological products such as the local weather research (e.g., Puysségur et al., 2007) and forecasting model (e.g., Yun et al., 2015), and global atmospheric reanalysis products (e.g., Doin et al., 2009; Jolivet et al., 2014; Walters et al., 2013). However, local meteorological data, spectrometer, and continuous GPS stations are rarely available for the time of each SAR acquisition: continuous GPS stations are often absent and are generally distributed with a coarse spatial density when considered globally; spectrometer observations from the Medium Resolution Imaging Spectrometer or the Moderate Resolution Imaging Spectroradiometer are not available at night, or over areas with cloud cover, and in the case of Medium Resolution Imaging Spectrometer were only available between 2002 and 2012. More importantly, spectrometer data can only be used to estimate the wet delay. As for regional numerical weather prediction models, although they have high temporal and spatial resolutions and can account for both the hydrostatic and wet delay, it has not been possible to obtain consistently robust results in a wide range of settings (Bekaert, Walters, et al., 2015; Cimini et al., 2012; Foster et al., 2013). In contrast, global weather models have the benefits of complete spatial coverage and data availability (Dee et al., 2011) and can also account for both the hydrostatic and wet delay. The latest high resolution European Centre for Medium-Range Weather Forecasts (HRES-ECMWF) analysis products have a much higher spatial resolution (16 km) when compared with previous global weather models (e.g., the spatial resolution of ERA Interim re-analysis products is 80 km), which could be beneficial for describing smaller-scale variation in tropospheric

delays. However, they are models that are still limited by the assimilation of observations to constrain their boundary conditions (Dee et al., 2016). In regions with sparse input data such as Western China, Africa, Western South America, and the polar regions, it is unclear of the performance of the models at their highest resolution. In addition, global weather models including the HRES-ECMWF suffer from timing issues as they are not sampled simultaneously with SAR acquisitions. This lack of synchronization is likely a contributing factor to the lack of consistently robust results from global weather models (Gong et al., 2015) also due to the relatively rapidly changing state of the troposphere.

There are two approaches to using the interferometric phase itself. Linear approaches assume a single relationship between phase and topography over the whole interferogram (e.g., Elliott et al., 2008; Lin et al., 2010; Wicks et al., 2002). The second assumes a power law correction relationship between phase and height (Bekaert, Hooper, et al., 2015; Hanssen, 2001), which allows for a spatial variability in tropospheric properties and estimation of long wavelength tropospheric signals as well as the topographically correlated component. This is particularly important for larger interferograms, where the assumption of consistent atmospheric properties across the whole image breaks down. However, measurements derived from balloon-sounding data (Bekaert, Hooper, et al., 2015) and weather model data (Figure 1) show that the actual observed and predicted patterns of differential tropospheric delays with height are more variable than a simple power law can sufficiently describe.

In this study, we describe a new approach, which combines the use of both external weather model data and the interferometric phase to address the limitations of using either approach individually. Rather than assuming a power law relationship, we use the HRES-ECMWF data to define the form of the relationship between tropospheric delay and height and then scale the magnitude of the delay to best match the interferometric phase. This can also be viewed as using the interferometric phase to refine the interpolation of the weather model in time and space. As the scaling factor will differ for the two tropospheric delays that contribute to an interferogram, we perform the scaling at each single epoch rather than for the interferometric tropospheric delay. We validate our scaling technique using simulations and Sentinel-1 C-band SAR data acquired over the central portion of the Altyn Tagh Fault in northern Tibet.

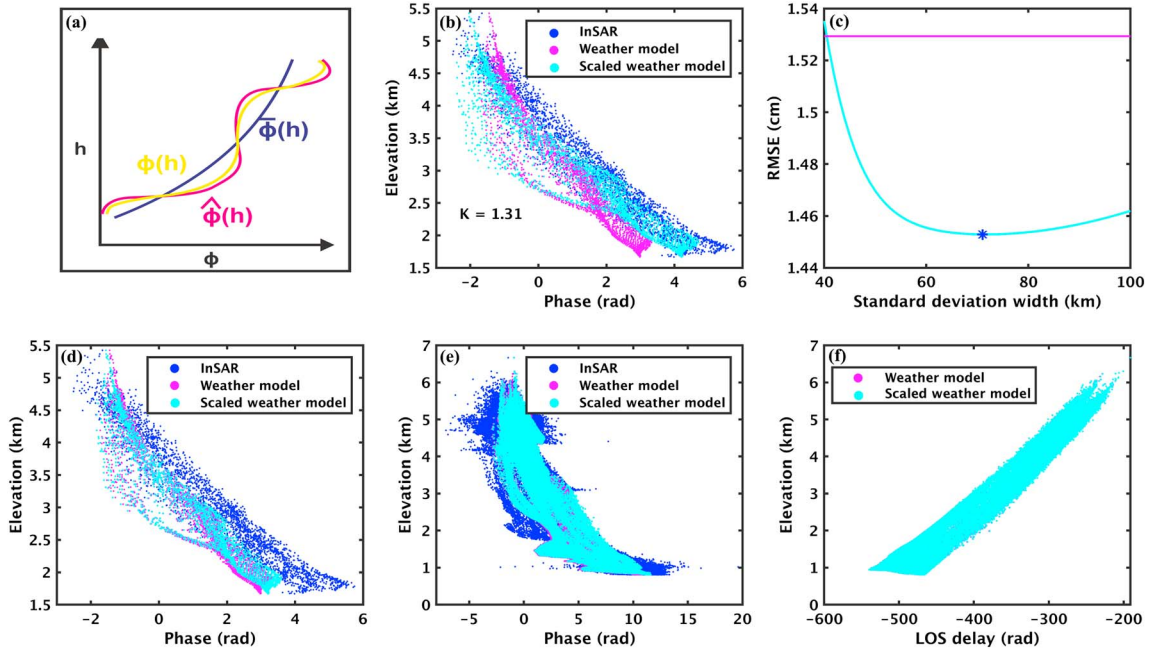


Figure 2. (a) An interpretive cartoon showing how the scaling operates. The blue curve represents the mean tropospheric delay for any given height. The magenta curve is the estimated tropospheric delay for a single acquisition time, and the yellow curve shows the same delay after scaling. Note that it is only the difference between the magenta and blue curves that is scaled. (b) The comparison between the weather model phase delay anomalies and the InSAR phase delay anomalies for the red patch in Figure 3a before and after scaling using the scaling factor estimated for the whole patch. (c) The RMSE variation between the scaled weather model phase delay anomalies (cyan curve) and the tropospheric phase delay anomalies estimated from two continuous GPS stations in Figure 4 when varying the standard deviation width of the Gaussian filter used for the scaling factor smoothing. The blue star indicates the optimal value of the standard deviation, which is 71 km and the corresponding RMSE is 1.45 cm. The magenta line represents the RMSE between the nonscaled weather model phase delay anomalies and the GPS anomalies, which is 1.53 cm. (d) The comparison between the weather model phase delay anomalies and the InSAR phase delay anomalies for the red patch in Figure 3a before and after scaling using the smoothed scaling factor. (e) The comparison between the InSAR phase delay anomalies and the weather model phase delay anomalies over the whole image. (f) The weather model delays in the LOS direction over the whole image before and after scaling. InSAR = interferometric synthetic aperture radar; LOS = line of sight; RMSE = root mean square error.

2. Spatially Varying Scaling Method

The phase delay through the troposphere depends on the refractivity, N , which can be divided into hydrostatic and wet components. At a specific height, h , the tropospheric phase delay ϕ_{tropo} corresponds to the integration of the refractivity between h and the top of the troposphere h_T in the radar line-of-sight (LOS) direction (Hanssen, 2001) as

$$N = N_{\text{hydr}} + N_{\text{wet}} = (k_1 \frac{P}{T})_{\text{hydr}} + (k_2' \frac{e}{T} + k_3 \frac{e}{T^2})_{\text{wet}} \quad (1)$$

$$\phi_{\text{tropo}} = \frac{-4\pi}{\lambda} \frac{10^{-6}}{\cos \theta} \int_h^{h_T} N dh \quad (2)$$

where P is total tropospheric pressure, T the temperature, e the partial pressure of water vapor, θ the radar incidence angle, λ the radar wavelength, k_1 , k_2' , and k_3 the constants that are empirically taken as 77.6, 23.3, and $3.75 \cdot 10^5$ K/hpa (Smith & Weintraub, 1953), respectively. Thus, given a weather model, such as HRES-ECMWF, we can derive a model LOS tropospheric delay for a given time. We use the approach of the triangle-based linear interpolation in space and linear interpolation in time to interpolate the weather model to every pixel of the master image and every acquisition time.

As the interferometric phase represents the difference in signal delay, it is only sensitive to the variability of the tropospheric delay with time and not the overall magnitude of the tropospheric delay. It is therefore the difference from the mean tropospheric delay that we aim to scale, where the mean delay is the average tropospheric delay in time for any given height (Figure 2a). For all epochs, we derive this difference from the mean phase delay, which we term the phase delay “anomaly,” using a minimum norm inversion, noting that there can be contributions other than the tropospheric delay in the resulting single epoch phase:

$$\delta\phi_{\text{InSAR}} = G^T(GG^T)^{-1}\phi_{\text{InSAR}} \quad (3)$$

where ϕ_{InSAR} is the vector of interferometric phase delays for a single pixel, $\delta\phi_{\text{InSAR}}$ the vector of estimated phase delay anomalies for every epoch, and G is the design matrix relating the relevant observation epochs for each interferogram. Note that throughout this manuscript, we use the term “phase delay anomaly” to refer to the portion of the interferometric phase allocated to a single epoch, whereas “phase delay” alone indicates the phase delay between two epochs. We incorporate only small baseline interferograms so as to minimize any decorrelation noise and contributions from deformation. The regularization of the minimum norm inversion of the interferograms will introduce smearing of the phase between epochs, due to imperfect resolution. To give the same smearing, we derive the single epoch anomalies from the weather model in the same way, by first calculating estimates of the phase delay for each interferogram from the single epoch delays and then inverting these using the minimum norm approach as

$$\delta\hat{\phi}_{\text{tropo}} = G^T(GG^T)^{-1}\hat{\phi}_{\text{tropo}} \quad (4)$$

where $\hat{\phi}_{\text{tropo}}$ is the vector of tropospheric phase delays for a single pixel in each interferogram, derived from the weather model, and $\delta\hat{\phi}_{\text{tropo}}$ is the vector of estimated phase delay anomalies for every epoch.

We assume that

$$\delta\phi_{\text{tropo}}(x, y, h) \approx K(x, y)\delta\hat{\phi}_{\text{tropo}}(x, y, h) \quad (5)$$

where $\delta\phi_{\text{tropo}}(x, y, h)$ is the actual tropospheric phase delay anomaly and $K(x, y)$ is a spatially varying scaling factor that is spatially smooth. We estimate values for $K(x, y)$ empirically using the single epoch phase delay anomalies derived from the interferograms, on the assumption that other interferometric components such as tectonic deformation, Digital Elevation Model (DEM) errors, and other sources of noise are not correlated with the scaled weather model phase anomalies.

2.1. Estimation of Scaling Factors

For each epoch, we divide the image into smaller windows and estimate the scaling factor, K , for each window. Because these single epoch phase maps ($\delta\phi_{\text{InSAR}}$) are relative to a local spatial reference, we cannot substitute them directly for $\delta\phi_{\text{tropo}}(x, y, h)$ in equation (5) but must include the unknown phase of the reference point. We estimate this reference independently for each patch, which has the effect of ignoring correlations between the InSAR and weather model anomalies at long spatial wavelengths. While using the correlation at long wavelengths could potentially improve the accuracy of the scaling, the long wavelength signals are often contaminated by nontropospheric errors from the ionosphere and orbital inaccuracy, which can bias the estimation.

For each patch we have

$$\delta\phi_{\text{InSAR}}^n = K_n\delta\hat{\phi}_{\text{tropo}}^n + C_n \quad (n \in \mathbb{N}) \quad (6)$$

where K_n and C_n are the scaling factor and the constant shift for the patch n that we estimate using least squares. To ensure a sufficient number of scatterers for the inversion, we set the square window size as 50 km (Figure 3a). However, as we smooth the scaling factor spatially in the next step, the final result is not strongly dependent on the choice of window size. Figure 3c shows the estimated scaling factors for a representative single epoch.

2.2. Scaling Factor Smoothing

The accuracy of the estimated scaling factor depends on the signal-to-noise ratio of the weather model anomalies. Therefore, we define a variance ratio to weight each patch as

$$W_{\text{var}}^n = \frac{\sigma_{\text{tropo}}^2(n)}{\sigma_{\text{res}}^2(n)} \quad (n \in \mathbb{N}) \quad (7)$$

where $\sigma_{\text{tropo}}^2(n)$ is the variance of the weather model delay anomalies in the patch n , representing the signal, and $\sigma_{\text{res}}^2(n)$ is the variance of the differences between the weather model delay anomalies and the InSAR phase delay anomalies in the patch n , representing the noise. For $\sigma_{\text{res}}^2(n)$, we also tried using the variance of the difference after scaling of the weather model, but this led to an increase in the mean velocity standard deviation from 2.6 to 3.4 mm/year.

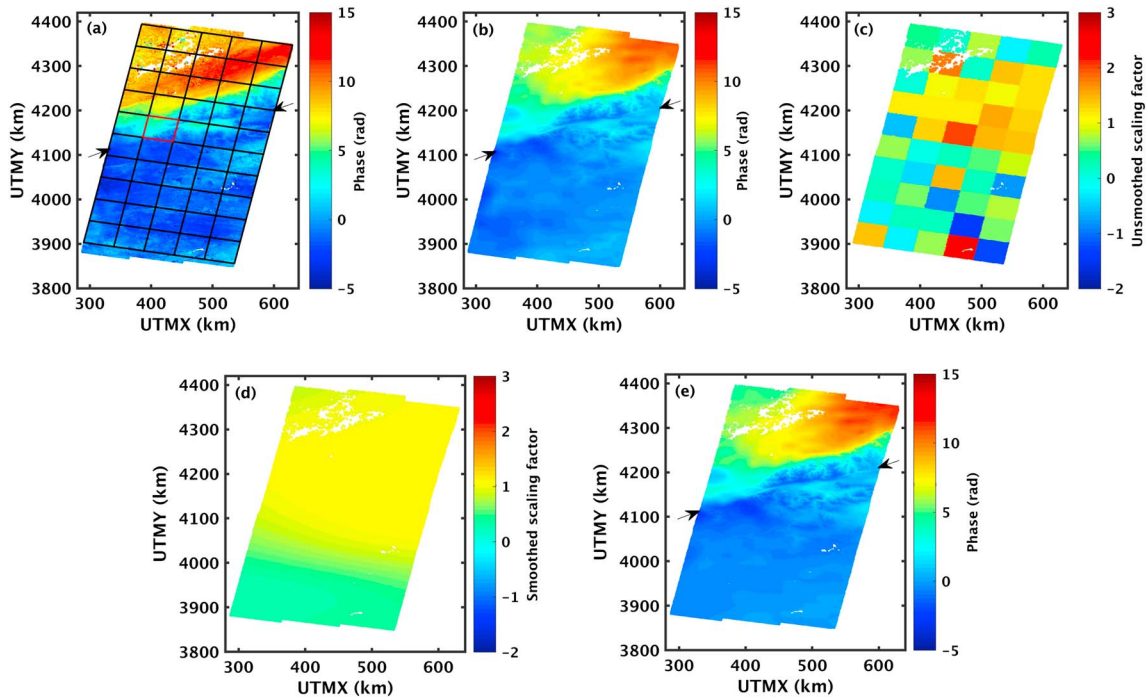


Figure 3. Example results of the scaling method applied to our testing area across the Altyn Tagh Fault. (a, b) The InSAR phase delay anomalies and weather model tropospheric phase delay anomalies, respectively, estimated using the minimum norm approach for a typical epoch, that of 17 May 2016. The black arrows indicate the fault orientation. The overlapped grid in (a) is rotated to the heading direction of the satellite, and each patch is completely within the SAR area so as to make sure the number of points in each patch is similar. (c) The scaling factors of all patches. (d) The spatial pattern of the spatially varying smoothed scaling factors. (e) The scaled tropospheric phase delay anomalies.

As the scaling is expected to vary spatially, we also estimate a distance weight for each pixel using a Gaussian filter as

$$W_{\text{dis}}^n(x, y) = \frac{1}{2\pi\sigma_d^2} \exp\left(-\frac{(x-X_n)^2 + (y-Y_n)^2}{2\sigma_d^2}\right) \quad (n \in \mathbb{N}) \quad (8)$$

where (X_n, Y_n) is the central coordinate of the window n and σ_d is the standard deviation width of the Gaussian filter. We then determine a scaling factor for each pixel as

$$K(x, y) = \sum_{n=1}^N \{K_n \cdot W_{\text{var}}^n \cdot W_{\text{dis}}^n(x, y)\} \quad (n \in \mathbb{N}) \quad (9)$$

Since the spatial pattern of the smoothed scaling factors is strongly dependent upon the Gaussian smoothing width σ_d , we optimize it using the tropospheric delays estimated from two continuous GPS stations (Figure 4). The total zenith tropospheric delay (ZTD) was processed with the GAMIT software (Liang et al., 2013), which parametrizes the ZTD for each station as a stochastic variation from the Saastamoinen model, with a piecewise linear function over the span of the observations (Herring et al., 2015). Taking the 2-hourly estimates of the ZTD, we estimate the delay at each SAR acquisition time using spline interpolation and transform into LOS delay. We then difference the single epoch values to give the delay for each interferogram time span and invert using the minimum norm approach to give anomaly values for each epoch (Table S1 in the supporting information). We scale the tropospheric delay anomalies estimated from the HRES-ECMWF data using different values for σ_d and compare these to the delay anomalies derived from the GPS data. Note that in the comparison, we select a continuous GPS station as the reference point and so the comparison is based on the relative tropospheric delay. The optimal σ_d is chosen as the value with a minimum root mean square error (RMSE) (Figure 2c). For regions without any continuous GPS stations, it will not be possible to estimate the optimal Gaussian smoothing width. However, the RMSE between the weather model and the GPS measurements varies little when the smoothing width changes over a broad range between 50 and 100 km, so using a default value of 71 km is likely to be fine in most cases. Figures 2b and 2d show the scaled

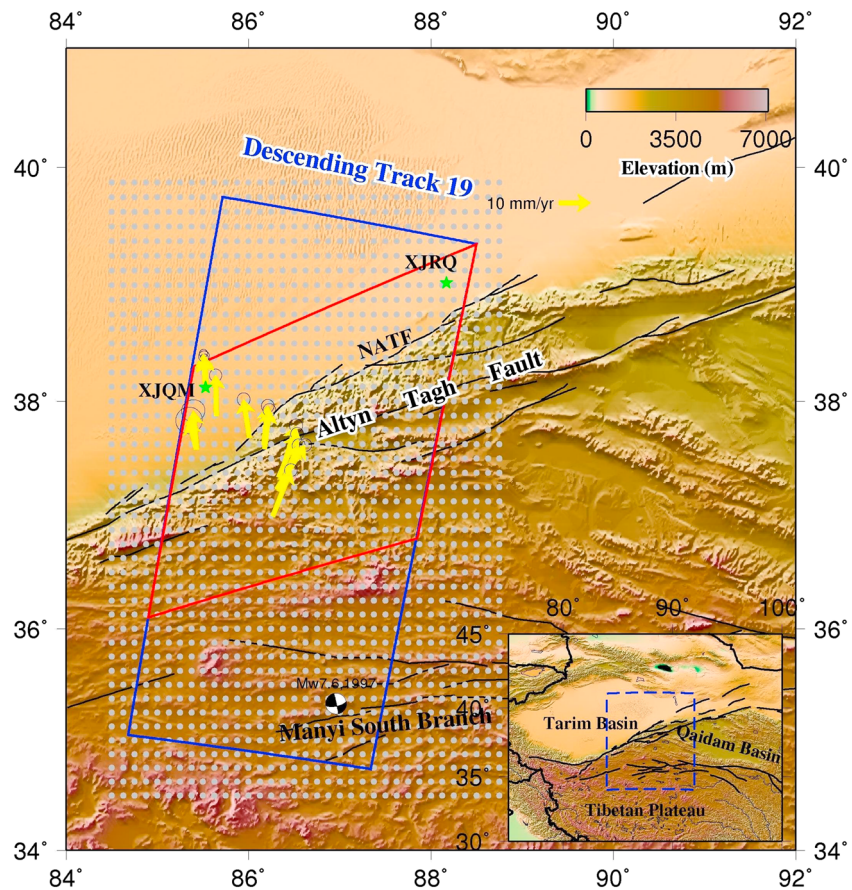


Figure 4. Map of the scaling method study region over the Altyn Tagh Fault zone, Tibet. The blue rectangle represents the extent of SAR data coverage. Gray dots indicate the high resolution European Centre for Medium-Range Weather Forecasts points used for tropospheric delay corrections of which the spatial resolution is 16 km. Green stars show the location of the only two available continuous GPS stations within the SAR image area (Liang et al., 2013). Yellow arrows indicate velocities of available campaign GPS stations near the fault within the InSAR area (He, Lu, et al., 2013; Liang et al., 2013). All of the GPS velocities are within the Eurasia reference frame, with uncertainties plotted at 95% confidence level. The red parallelogram indicates the outline of deforming region that we mask out before estimating phase ramps. The background shows the elevation of the study region derived from the Shuttle Radar Topography Mission 3-arc seconds data (Farr et al., 2007), which is also applied to the subsequent figures.

results for the red patch in Figure 3a before and after smoothing of the scaling factor. Although the scaling factors estimated for a single patch can have large errors with absolute values much greater than one (Figure 3c), these patches are downweighted in the smoothing process, leading to smoothed factors close to 1 (Figure 3d).

Using the smoothed spatially varying scaling factors, we scale the tropospheric phase delay anomalies estimated from the HRES-ECMWF for each epoch (Figure 3e) and calculate the scaled interferometric tropospheric delays from these. The scaled tropospheric phase delay anomalies are more consistent with the InSAR phase delay anomalies (Figure 2e), as is to be expected. As the scaling is implemented on the tropospheric phase delay anomalies, the absolute change to the total weather model delay resulting from the scaling is small (Figure 2f). In the next section, we test how robust the approach is in the presence of tectonic deformation.

3. Simulated Test Cases

To test the ability of the method to separate deformation from tropospheric signals, we simulated a subvertical, strike-slip (M_w 6.7) earthquake (details in Table 1) on the northern strand of the Altyn Tagh Fault in Northern Tibet (Figure 4), a region that is strongly contaminated by the variation in tropospheric delay across the step in relief. We chose a subvertical, strike-slip earthquake because the Altyn Tagh Fault is of this

Table 1
Parameters of the Simulated Earthquake Used

Parameter	Value
Fault center	87.3°E, 38.3°N
Magnitude (M_w)	6.7
Strike	66°
Top depth	2 km
Dip	60°
Bottom depth	15 km
Rake	0°
Slip	1 m
Length	25 km
LOS vector unit (E, N, U)	[0.6557, -0.1147, 0.7447]

Note. LOS = line of sight.

type. We determined the depth of rupture based on the previous measurements for the locking depth of the fault (Elliott et al., 2008; He, Lu, et al., 2013). We set the earthquake magnitude to be sufficiently large that the spatial coverage of the simulated signal would be larger than the applied Gaussian smoothing size. We added an example of real noise to the simulated deformation, including tropospheric signal, as described in the following paragraph.

We processed 19 SAR images acquired by Sentinel-1 on descending track 19 between October 2014 and September 2016 and generated 53 small baseline interferograms using the Looking inside the Continents from Space SAR software package (Figure S1; Wright et al., 2016). We used the Stanford Method for Persistent Scatterers software package (Hooper, 2008) to remove the incoherent pixels and unwrap the phase of stable scatterers in the small baseline interferograms with a 3-D unwrapping method (Hooper, 2010). After phase unwrapping, we checked the phase closure and corrected unwrapping errors manually. Significant interferometric processing parameters are summarized in Table 2. Based on the 53 unwrapped small baseline interferograms, we solved for InSAR phase delay anomalies for each epoch using the minimum

norm approach (Figure S2). We added the simulated earthquake signal (Figure 5a) to the InSAR phase delay anomaly for the 14 September 2016 and then generated a 24-day interferogram with the InSAR phase delay anomaly at the epoch 21 August 2016 (Figure 5b). We selected this interferometric pair because it is strongly influenced by tropospheric delays and the short interval of the interferometric plane limits contamination from any real interseismic tectonic deformation.

We processed the HRES-ECMWF pressure level data using the Toolbox for Reducing Atmospheric InSAR Noise (TRAIN version 1; Bekaert, Walters, et al., 2015). HRES-ECMWF has a spatial resolution of 16 km, at 6-hr intervals, and provides parameters of temperature, pressure, relative humidity, and geopotential on 25 pressure levels. Within the TRAIN software, the HRES-ECMWF integrated refractivity is linearly interpolated to match the SAR acquisition time. Figure S3 shows the estimated tropospheric phase delay anomalies for the two selected epochs. We then used the InSAR phase delay anomalies associated with the simulated interferogram to scale the weather model anomalies using a 50-km by 50-km grid. The simulated earthquake signal above 2 mm covers 27 of 50 square patches in total (Figure 5a) and so the spatial coverage is much larger than the applied Gaussian smoothing size, which is 71 km. Finally, as the real interferometric phase that we added will also include long wavelength errors due to ionospheric signal and orbital inaccuracy, we estimate a phase ramp from the nondeforming region shown in Figure 4 and subtract it.

Figure 5c shows the results after correction using the original HRES-ECMWF. Much of the noise has been reduced when compared to Figure 5b. However, when using the scaled tropospheric delays, shown in Figure 5d, the noise is reduced still further, with the RMSE between the corrected signal and the deformation signal alone dropping from 1.9 to 0.8 rad. Importantly, the scaling estimation process does not result in an obvious reduction of the deformation signal.

As the magnitude and spatial extent of interseismic slip is very different to coseismic motion, we also simulated 10-mm left-lateral strike-slip motion from 15 km downward along the central branch of the Altyn Tagh

Table 2
InSAR Processing Parameters

InSAR processing		Small baseline analysis	
Parameter	Value	Parameter	Value
Wavelength	0.0555 m	Number of patches	27
SRTM DEM	90 m	Unwrap grid size	1,200 m
Multilook factor	20 × 4	Merge resample size	1,000 m
		Merge σ	1 rad

Note. InSAR = interferometric synthetic aperture radar; SRTM = shuttle radar topography mission; DEM = digital elevation model.

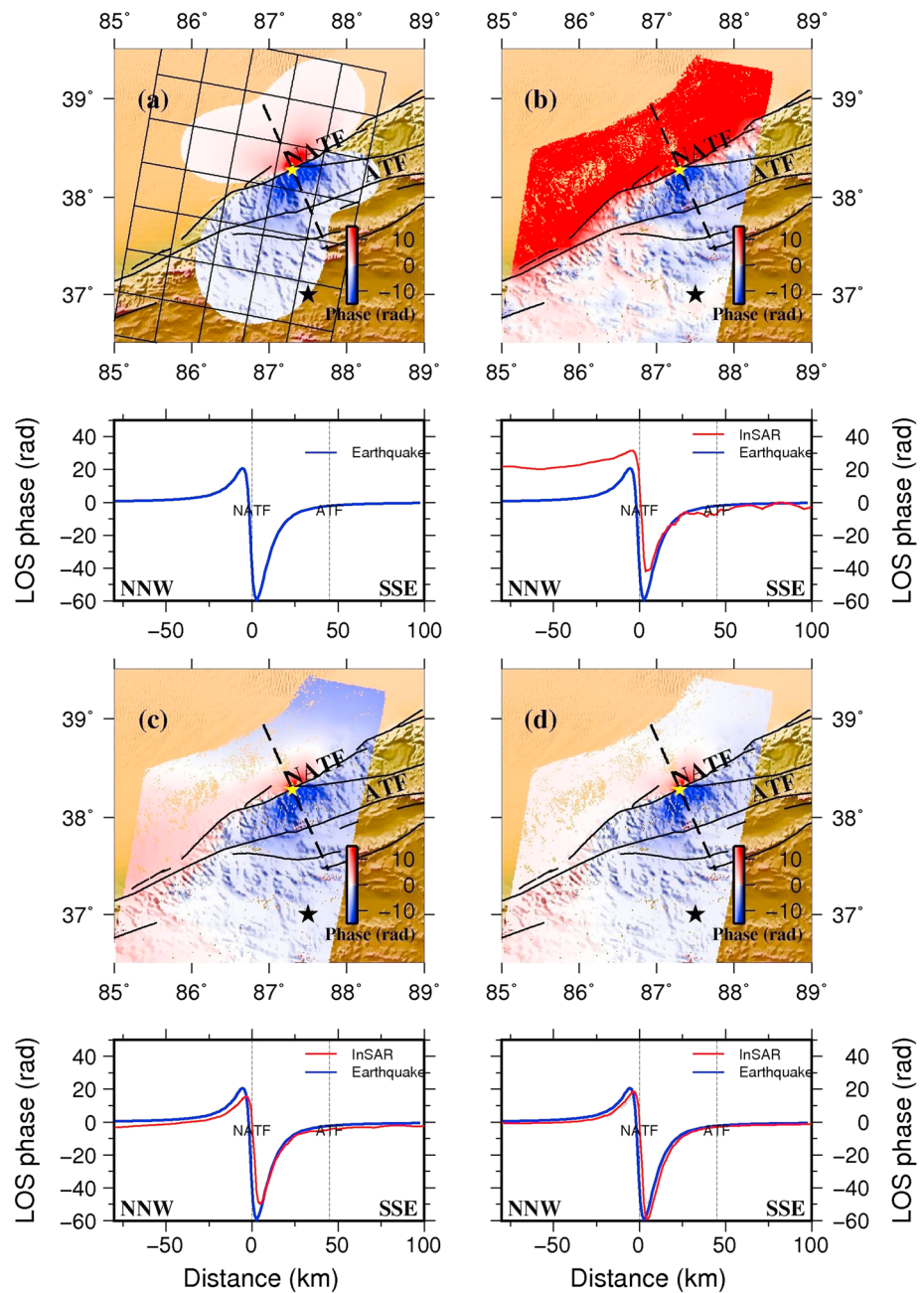


Figure 5. Tropospheric correction results for a 24-day interferogram to which deformation from a simulated earthquake has been added: (a) the simulated earthquake signal and the grid of windows used for calculating the scaling factor, K , (b) the uncorrected interferogram, (c) the interferogram corrected using the original high resolution European Centre for Medium-Range Weather Forecasts and with an estimated phase ramp subtracted, and (d) the interferogram corrected with the scaled tropospheric delays from high resolution European Centre for Medium-Range Weather Forecasts and with an estimated phase ramp subtracted. For each panel, positive values indicate motion away from the satellite. The red lines in the panels below indicate the interferometric phase along the black dashed profile. The blue lines represent the simulated earthquake signals. The fault center (yellow star) is at the 0-km profile distance. The black star indicates the InSAR reference point. InSAR = interferometric synthetic aperture radar; LOS = line of sight.

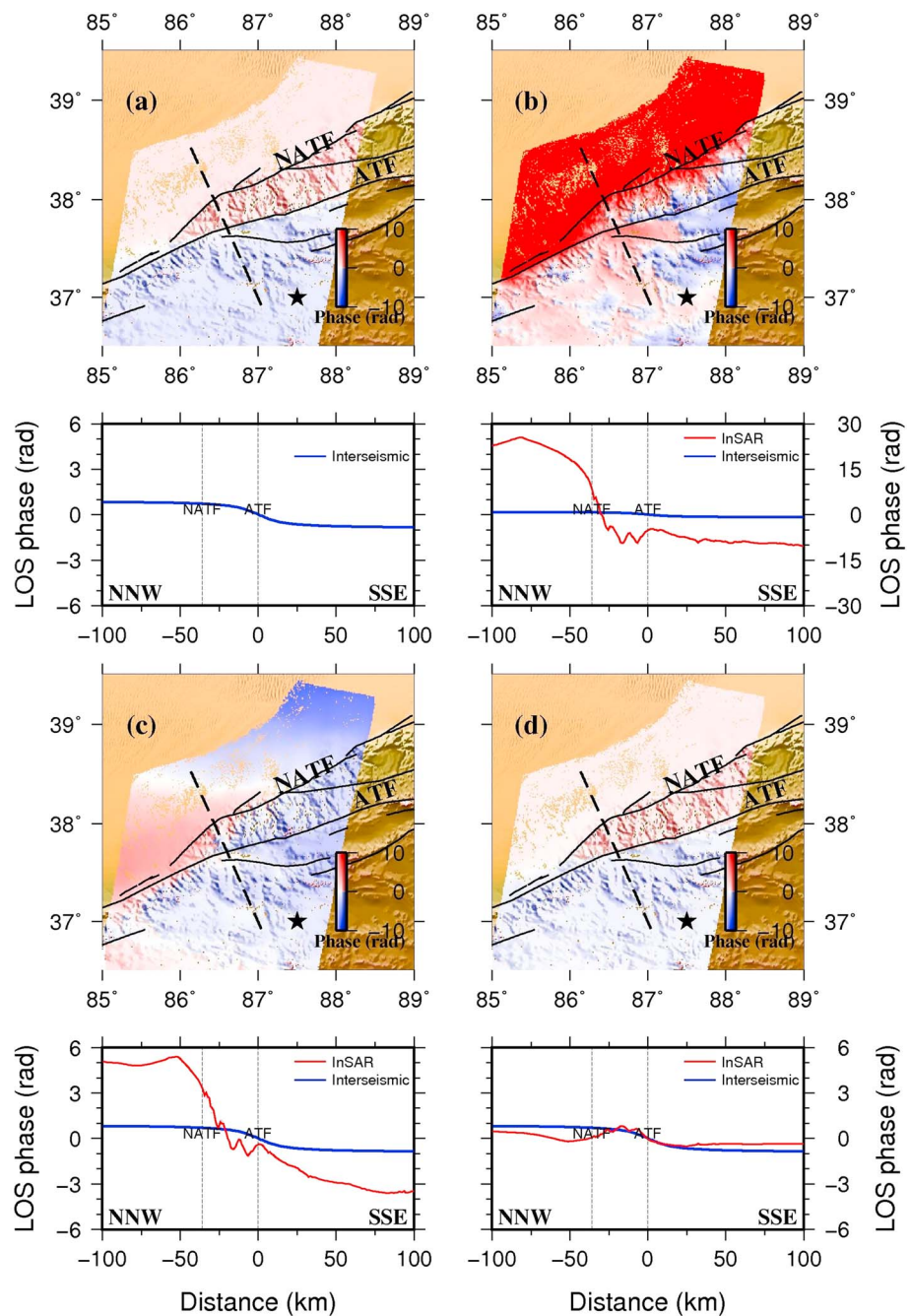


Figure 6. Tropospheric correction results for a 24-day interferogram to which deformation from a simulated interseismic signal has been added: (a) the simulated interseismic deformation signal, (b) the uncorrected interferogram, (c) the interferogram corrected with the original high resolution European Centre for Medium-Range Weather Forecasts and with an estimated phase ramp subtracted, and (d) the interferogram corrected with the scaled tropospheric delays and with an estimated phase ramp subtracted. For each panel, positive values indicate motion away from the satellite. The red lines in the panels below indicate the interferometric phase along the black dashed profile. The blue line represents the simulated interseismic signals. The fault dislocation is at 0-km distance. The black star indicates the interferometric synthetic aperture radar reference point. InSAR = interferometric synthetic aperture radar; LOS = line of sight.

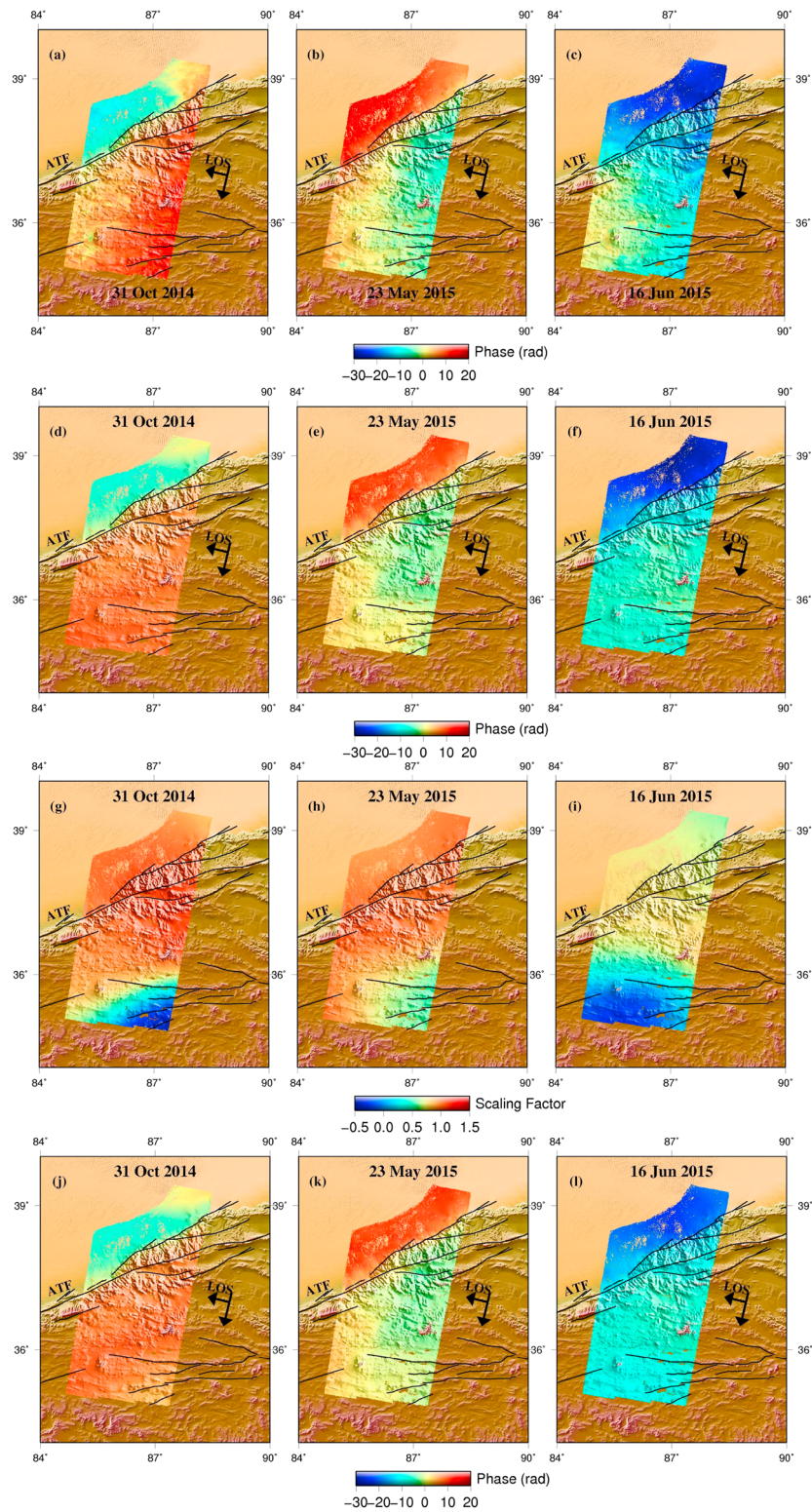


Figure 7. (a–c) InSAR phase delay anomalies for three selected epochs, estimated from a small baseline interferogram network using a minimum norm constraint. (d–f) Tropospheric phase delay anomalies for the same epochs estimated from high resolution European Centre for Medium-Range Weather Forecasts using the minimum norm solution. (g–i) The smoothed scaling factor applied to the high resolution European Centre for Medium-Range Weather Forecasts correction, for the same epochs. (j–l) The scaled tropospheric phase delay anomalies for the same epochs. The phase value in each epoch is referenced to the interferometric synthetic aperture radar phase delay anomaly of the corresponding epoch for the comparison. LOS = line of sight.

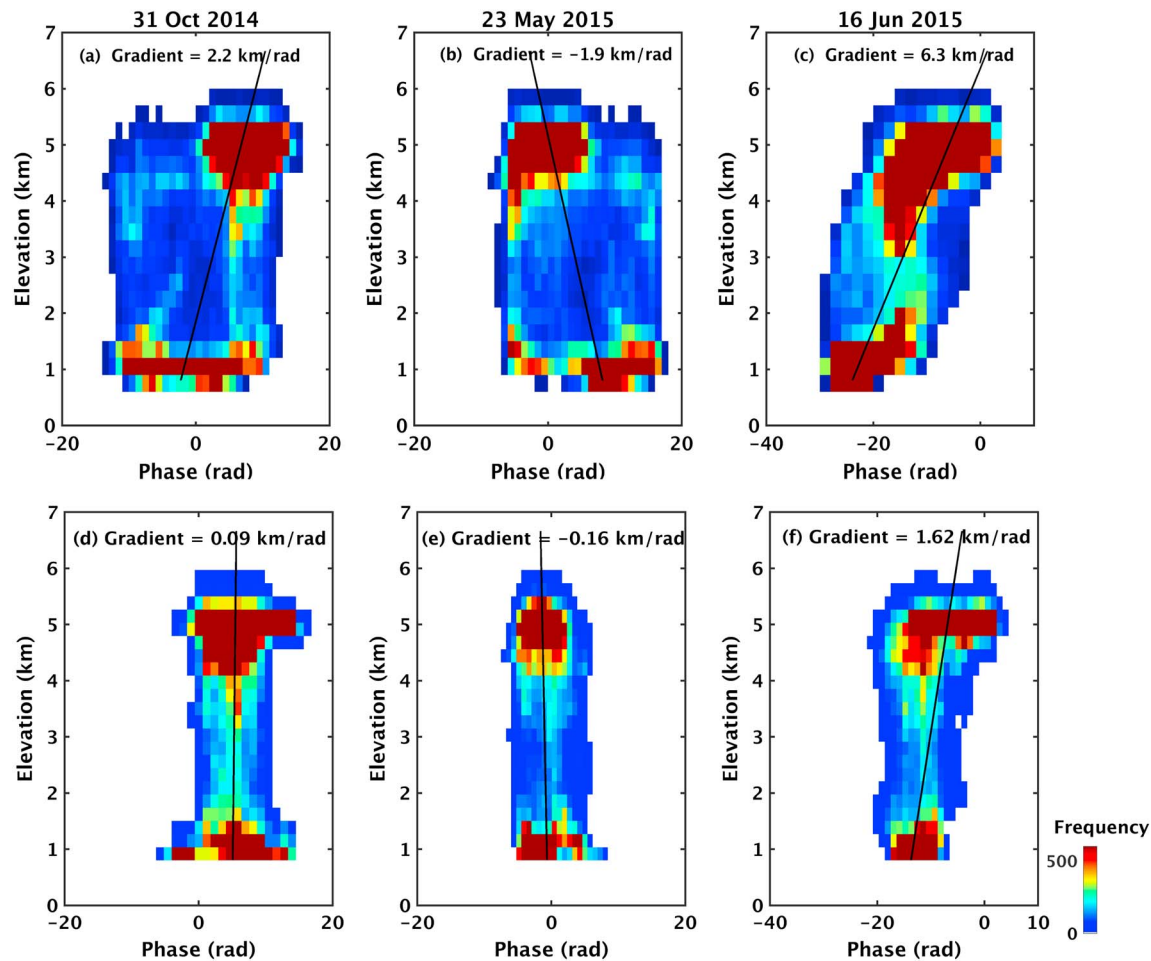


Figure 8. Histograms of the interferometric synthetic aperture radar phase delay anomalies versus topography for the same three epochs shown in Figure 7 before (a–c) and after (d–f) tropospheric corrections with the scaled weather model anomalies. The black lines are the best fitting linear function, shown for reference.

Fault and added it to the same 24-day interferogram (Figure 6). This simulation approximates a 1-year interferogram with a slip rate of 10 mm/year. Although the corrected results are not as clean as in the seismic case, due to the lower magnitude of the signal, the isolation of deformation shows a marked improvement over the unscaled case with the RMSE between the corrected signal and the deformation signal alone dropping from 1.8 to 0.6 rad.

4. Case Study

To test our algorithm on real data, we applied the scaling method to interferograms over the central portion of the Altyn Tagh Fault (Figure 4). The Altyn Tagh Fault is one of the major tectonic structures in northern Tibet, and accurate determination of its slip rate has significant implications for the interpretation of tectonic processes across the Tibetan Plateau region (Searle et al., 2011; Tapponnier et al., 2001). However, as the fault is located at the border between the low Tarim Basin and the high Tibetan Plateau, the interseismic deformation signals are strongly masked by the tropospheric delays resulting from the 6,000-m topographic relief across it.

From the 19 SAR images that we processed (Figure S2), we selected three epochs that are strongly influenced by the tropospheric delays as examples to show (Figure 7), which are 31 October 2014, 23 May 2015, and 16 June 2015. The InSAR phase delay anomalies are highly correlated with the topography (Figures 8a–8c and S4), which implies the existence of strong tropospheric delays. We estimated the smoothed spatially varying scaling factor for every epoch (Figures 7g–7i and S5) and then scaled the original weather model anomalies (Figures 7j–7l and S6). After removing the scaled tropospheric delay anomalies from the InSAR

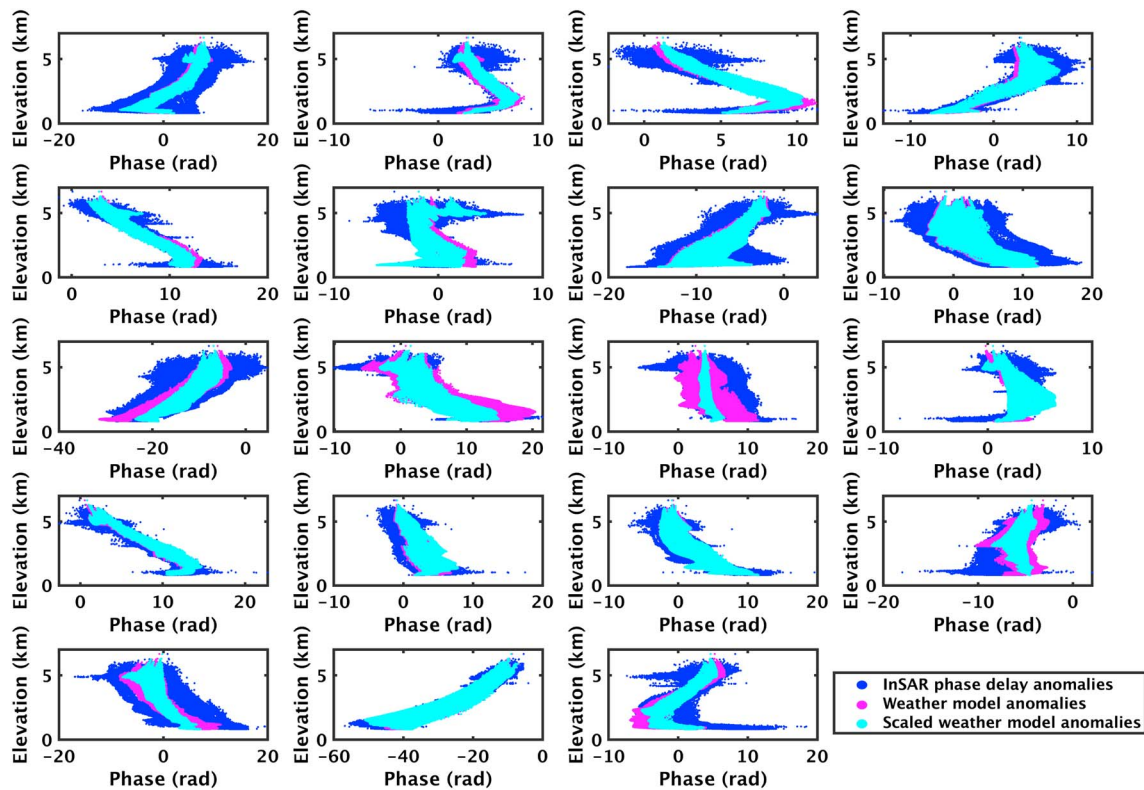


Figure 9. Comparisons of the original and scaled weather model phase delay anomalies to the InSAR phase delay anomalies, for each epoch. InSAR = interferometric synthetic aperture radar.

phase delay anomalies in each epoch, the phase no longer has strong correlations with the topography (Figures S7 and 8d–8f). Although we deliberately omit the long wavelength component during the estimation of the scaling factors, this does not prevent the application of the scaling from resulting in a gradient in the tropospheric anomalies. Therefore, the long wavelength differences between InSAR phase delay anomalies and the scaled tropospheric phase delay anomalies suggest that nontropospheric long wavelength signal exists in the InSAR data.

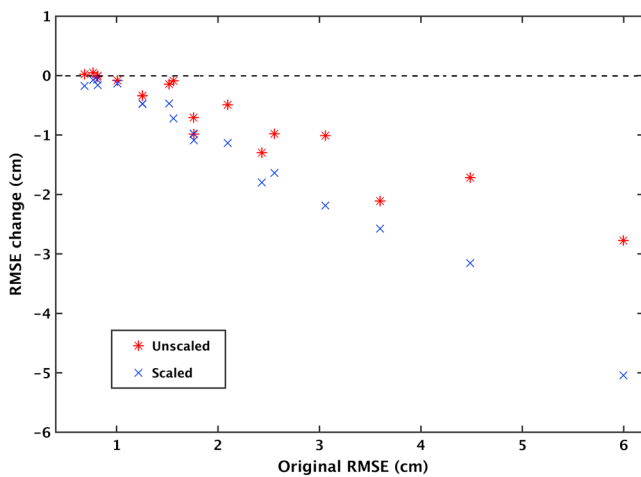


Figure 10. RMSE comparisons of deramped single master interferograms before and after tropospheric corrections. The RMSE of all interferograms reduces after correction with the scaled high resolution European Centre for Medium-Range Weather Forecasts, even for the two interferograms for which the RMSE increases after correction with the original HRES-ECMWF. The master date of the interferograms is 17 November 2015. RMSE = root mean square error.

In order to investigate whether the scaled weather anomalies are simply mimicking the InSAR phase delay anomalies, we calculated the correlation coefficient between the InSAR phase delay anomaly and the scaled weather model anomaly for each epoch and compared them to the correlation coefficient between the weather model anomaly and scaled weather model anomaly. The results (Figure S8) show that the scaled weather model data are more correlated with the original weather model products than the InSAR phase delay anomalies, for 18 of the 19 epochs. Figure 9 also indicates that the general characteristics of the weather model have been kept after the scaling.

We then generated 18 single master interferograms and subtracted the estimated tropospheric delays from each interferogram. For each tropospheric-corrected interferogram, we also subtracted a ramp estimated from the nondeforming region (Figure 4). The RMSE of the interferograms corrected using the scaled tropospheric delays drops 38% on average compared with the interferograms corrected using the original estimates derived from the HRES-ECMWF, with RMSE drops of 60% on average compared with the uncorrected interferograms (Figure 10).

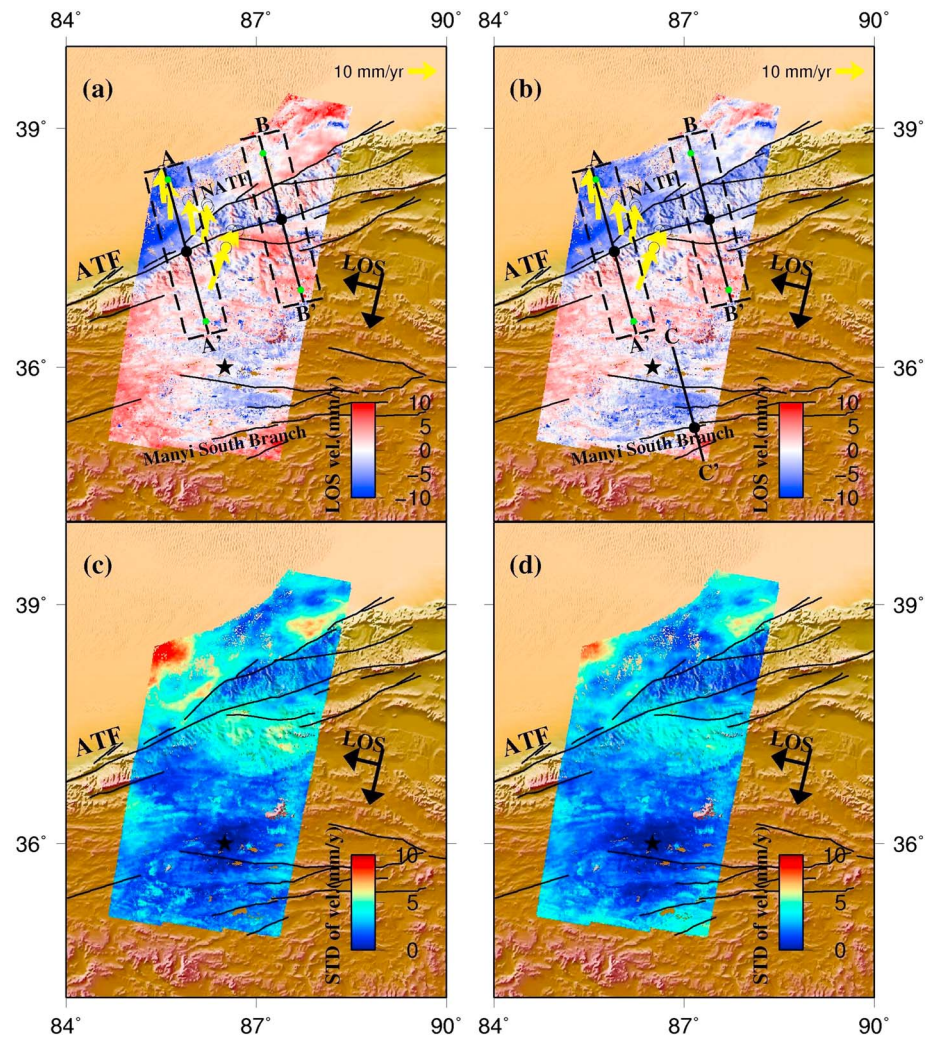


Figure 11. LOS annual velocity maps derived from the single master interferograms corrected with (a) the original and (b) the scaled tropospheric delays and their respective standard deviations (c and d) estimated by the percentile bootstrapping technique (e.g., Efron & Tibshirani, 1994). Incoherent scatterers in the northern sandy area were masked out. Positive values indicate motion toward the satellite and negative values indicate motion away from the satellite relative to the reference region (black star). Black lines A-A' and B-B' represent profiles which are perpendicular to the strike of the Altyn Tagh Fault with the center of 85.9°E, 37.5°N, 87.4°E, and 37.9°N, respectively, and a 120-km extension of each side of the fault. The black dash line indicates the extent of the velocity projection (swath width 30 km). Black line C-C' represents profile which is perpendicular to the Manyi south branch. Yellow arrows show velocities of available campaign GPS stations near the fault within the InSAR area (He, Lu, et al., 2013; Liang et al., 2013), which are in a Eurasia reference frame with uncertainties plotted at 95% confidence level. LOS = line of sight.

Based on the 18 tropospheric corrected and deramped single master interferograms, we calculated LOS velocities using the best linear unbiased solution (BLUE) (e.g., Puntanen et al., 2000). We calculated phase variances for each epoch from the variances of the tropospheric corrected and deramped interferograms with temporal baseline of less than 48 days, by least squares inversion. We then used these variances as the elements on the principal diagonal of the variance-covariance matrix in the BLUE inversion. Off-diagonal elements were set to zero since the noise of each epoch is considered to be independent. The velocity map derived from the interferograms after correction using the scaled tropospheric delays (Figure 11b) is clearly more consistent with left-lateral strike-slip deformation than that corrected using the original tropospheric delays, with motion north of the Altyn Tagh Fault more consistently away from the satellite and motion on the Plateau systematically toward. The mean standard deviation of velocities generated by bootstrapping the signal master time series also drops from 2.9 mm/year (Figure 11c) to 2.6 mm/year (Figure 11d).

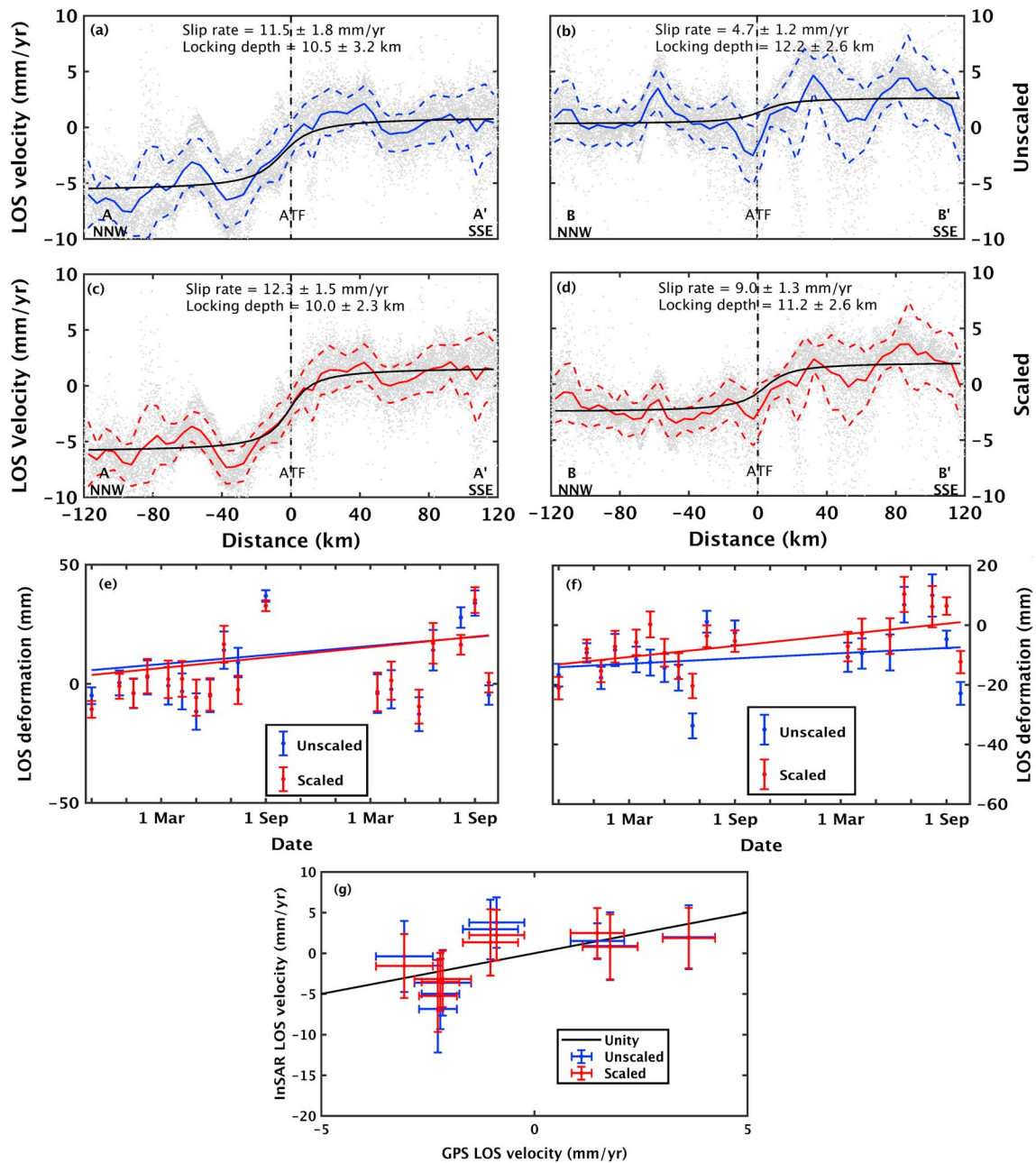


Figure 12. LOS InSAR velocities for profiles A-A' and B-B' in Figure 11: (a, b) velocities estimated from interferograms corrected using high resolution European Centre for Medium-Range Weather Forecasts and (c, d) velocities corrected by the scaled tropospheric delays. The red and blue full lines and dashed lines represent the average values and the $\pm 1\sigma$ of the profiles, respectively, calculated from 5-kmlong bins. The black full line represents the maximum likelihood solution for the interseismic deformation modeling estimated using a simulated annealing inversion. (e, f) The temporal evolution of deformation between two distant points along the profile A-A' and B-B', respectively (green points in Figures 11a and 11b). Error bars represent the $\pm 1\sigma$ spread. The measurements are much closer to a linear model in time (indicated by the blue and red lines) when corrected using the scaled tropospheric delays. (g) The LOS velocity comparison between the InSAR and surrounding campaign GPS measurements. The horizontal error bar represents the $\pm 1\sigma$ GPS errors, and the vertical error bar shows the InSAR errors from bootstrapping. Proximity to the black line, which marks equality between GPS and InSAR, implies that velocities match within error both before and after scaling, although errors are smaller after scaling. GPS = Global Positioning System; InSAR = interferometric synthetic aperture radar; LOS = line of sight.

As the campaign GPS data were not provided with vertical estimates, we projected GPS velocities estimated from measurements made at sites shown in Figure 11 to the LOS direction by assuming vertical deformation is negligible and then calculated the weighted mean offset from the InSAR results. We then added the offset to the InSAR measurements to tie them to the same reference frame as the GPS data, with Eurasia fixed. We projected the referenced InSAR velocities to two profiles, A-A' and B-B', which are perpendicular to the fault strike, within a 30-km width (Figures 11a and 11b). We used a simple elastic half-space model (Savage & Burford, 1973) to estimate the slip rate and the locking depth for profile A-A' and B-B'. Using the original HRES-ECMWF corrections, we found slip rates of 11.5 ± 1.8 and 4.7 ± 1.2 mm/year and 10.5 ± 3.2 and 12.2 ± 2.6 km for the locking depth (Figures 12a and 12b). Errors represent 2σ errors estimated using the percentile bootstrap method (e.g., Efron & Tibshirani, 1994). Using velocities estimated from the interferograms corrected using the scaled HRES-ECMWF, we found slip rates of 12.3 ± 1.5 and 9.0 ± 1.3 mm/year and the locking depth of 10.0 ± 2.3 and 11.2 ± 2.6 km (Figures 12c and 12d), which are more consistent with previous modeling of GPS measurements around this region, giving a slip rate of $9.0^{-3.2}_{+4.4}$ mm/year (He, Vernant, et al., 2013).

We calculated the time series of relative LOS displacement between two points located 200 km apart, either side of the Altyn Tagh Fault along profile A-A' and B-B', respectively, from the interferograms corrected using both the original and the scaled tropospheric delays (Figures 12e and 12f). Both time series show less scatter after scaling implying that the tropospheric delays have been reduced. The left-lateral strike-slip deformation across the fault also becomes apparent for the time series along the profile B-B', where the scaling has more impact. Comparing the InSAR estimates to the independent GPS measurements (He, Lu, et al., 2013; Liang et al., 2013), the RMS misfit drops from 3.0 to 1.9 mm/year with application of the additional scaling correction (Figure 12g).

5. Discussion

In this study, we use the HRES-ECMWF data rather than a power law relationship to define the form of the relationship between tropospheric delay and height and then scale the magnitude of the delay to best match the interferometric phase. The results demonstrate that our method is able to better isolate deformation across the Altyn Tagh Fault zone.

Although the magnitudes of the estimated scaling factors are generally close to 1, indicating that significant information is being provided to the correction from the weather model, there are cases where it is very small (Figure S5). This tends to be where the HRES-ECMWF anomaly values are themselves small (Figure S10) and therefore have a lower signal-to-noise ratio. The effect of a small scaling factor is to reduce the influence of the HRES-ECMWF correction still further, which makes sense if it is dominated by the prediction error.

To investigate what proportion of the information contained in the weather model is still being used after the scaling, we randomized the weather model epochs (Table S2) and reapplied our method, using the randomized weather model products to derive the velocity map. The comparison between the InSAR results and the surrounding campaign GPS measurements shows that randomizing the weather model makes the result much worse (Figure S11). This demonstrates that important information from the weather model is being utilized in the scaling process and that the method does not simply reduce all of the signal in the interferograms, which would include the deformation.

For some epochs, the difference between the scaled weather model anomalies and original weather model anomalies has a long wavelength component which could be contributed to by ionospheric effects or orbital errors. To test whether our algorithm artificially removes long wavelength errors due to nontropospheric contributions, we added a simulated ramp to the original InSAR phase delay anomalies and reestimated the scaled weather model anomaly. The results show that the added ramp does not dominate the values of the scaling factor (Figure S12).

We also applied the power law method (Bekaert, Hooper, et al., 2015) to the same region within the TRAIN (Table S3) and found that the average RMSE of the 18 single master interferograms increases by 20% after tropospheric corrections. The LOS annual velocity derived from the interferograms corrected with the power law method shows that it is unable to separate the left-lateral strike-slip deformation across the Altyn Tagh Fault (Figure S13). We calculated the time series of relative LOS displacement derived from the interferograms corrected using the power law method between two distant points along the profile B-B' (Figures 11a

and 11b), whereas the results (Figure S14) indicate an opposite (right-lateral) motion trend across the fault. It is possible that the failure of the power law method is caused by the extremely high relief in this region.

As well as the motion across the Altyn Tagh Fault, the final LOS annual velocity map reveals an approximately 5-mm/year velocity gradient across the Manyi south branch (Profile C-C' in Figure 11b), where a M_w 7.6 earthquake occurred in 1997; Funning et al., 2007; Wang et al., 2007). We compared the LOS velocity profile (Figure S15) to the interseismic deformation estimates prior to the earthquake (Bell et al., 2011) and the measurements of the postseismic motion following the earthquake (Ryder et al., 2007), respectively. We find that the current deformation rate across the Manyi south branch is smaller than the rate during the 4 years immediately following the earthquake, which was around 1 cm/year but still larger than the estimated interseismic rate of 3 mm/year, indicating that the elevated signals are caused by the postseismic motion, 20 years after the event.

The InSAR data (Figure 11b) are noisy for some areas in the Plateau region, which is likely to be caused by the permafrost (Daout et al., 2017). The data also show a step in velocity over the southern Tarim, which may be associated with vertical deformation in this region.

While we have tested this method on tectonic applications, we expect it to work well for other applications also, such as volcanic deformation and anthropogenic subsidence. We do not expect it to be unduly influenced by the correlation of deformation and topography that is sometimes present in the case of volcanic deformation as the method does not estimate the troposphere directly from its correlation with topography and the scaling factor that is estimated from a wider area than just the volcano itself. The simulated earthquake scenario (Figure 5) is similar to the volcanic scenario, where deformation correlates with topography, but the tropospheric signal is nevertheless well retrieved. However, the method could potentially be enhanced by simultaneously estimating a model for deformation while estimating the scaling parameter.

6. Conclusions

We have developed a novel approach for reducing tropospheric effects in InSAR which combines the use of both external weather model data and the interferometric phase. We use the HRES-ECMWF data to define the form of the relationship between tropospheric delay and height and then scale the magnitude of the delay to best match the interferometric phase. We tested our new method on simulated data, and the results demonstrate that it can separate both coseismic and interseismic signals from an interferogram contaminated by strong tropospheric delays. We also applied the method to the central portion of the Altyn Tagh Fault in the northern Tibet. We find that our method better reduces the strong tropospheric delays in this region, leading to clearer long wavelength deformation signals. These results suggest that the extra scaling step should be applied wherever weather model data are being used to correct interferograms.

References

- Ainscoe, E., Elliott, J. R., Copley, A., Craig, T., Li, T., Parsons, B., & Walker, R. (2017). Blind thrusting, surface folding, and the development of geological structure in the M_w 6.3 2015 Pishan (China) Earthquake. *Journal of Geophysical Research: Solid Earth*, *122*, 9359–9382. <https://doi.org/10.1002/2017JB014268>
- Bekaert, D., Hooper, A., & Wright, T. (2015). A spatially variable power law tropospheric correction technique for InSAR data. *Journal of Geophysical Research: Solid Earth*, *120*, 1345–1356. <https://doi.org/10.1002/2014JB011558>
- Bekaert, D., Walters, R., Wright, T., Hooper, A., & Parker, D. (2015). Statistical comparison of InSAR tropospheric correction techniques. *Remote Sensing of Environment*, *170*, 40–47.
- Bell, M., Elliott, J. R., & Parsons, B. (2011). Interseismic strain accumulation across the Manyi fault (Tibet) prior to the 1997 M_w 7.6 earthquake. *Geophysical Research Letters*, *38*, L24302. <https://doi.org/10.1029/2011GL049762>
- Chaussard, E., Wdowinski, S., Cabral-Cano, E., & Amelung, F. (2014). Land subsidence in central Mexico detected by ALOS InSAR time series. *Remote Sensing of Environment*, *140*, 94–106.
- Cimini, D., Pierdicca, N., Pichelli, E., Ferretti, R., Mattioli, V., Bonafoni, S., et al. (2012). On the accuracy of integrated water vapor observations and the potential for mitigating electromagnetic path delay error in InSAR. *Atmospheric Measurement Techniques*, *5*(5), 1015.
- Daout, S., Doin, M.-P., Peltzer, G., Lasserre, C., Socquet, A., Volat, M., & Sudhaus, H. (2018). Strain partitioning and present-day fault kinematics in NW Tibet from Envisat SAR interferometry. *Journal of Geophysical Research: Solid Earth*, *123*, 2462–2483. <https://doi.org/10.1002/2017JB015020>
- Daout, S., Doin, M.-P., Peltzer, G., Lasserre, C., Sudhaus, H., & Socquet, A. (2017). Large-scale InSAR monitoring of permafrost freeze-thaw cycles on the Tibetan Plateau. *Geophysical Research Letters*, *44*, 901–909. <https://doi.org/10.1002/2016GL070781>
- Dee, D. P., Fasullo, J., Shea, D., & National Center for Atmospheric Research Staff. (2016). *The Climate Data Guide: Atmospheric Reanalysis: Overview & Comparison Tables*. Boulder, CO: National Center for Atmospheric Research. Retrieved from <https://climatedataguide.ucar.edu/climate-data/atmospheric-reanalysis-overview-comparison-tables>. Accessed June, 1, 2017.

Acknowledgments

We acknowledge European Centre for Medium-Range Weather Forecasts (ECMWF) and Dr. Paola Crippa who was at the Newcastle University for their operational HRES-ECMWF pressure level products (<https://www.ecmwf.int/en/forecasts/datasets/set-i>). We thank Dr. Shiming Liang at the Institute of Geology of the China Earthquake Administration for providing us the continuous GPS data (<https://doi.org/10.1002/2013JB010503>). Sentinel-1 images were provided freely by the Sentinels Scientific Data Hub of the European Space Agency (ESA; <https://scihub.copernicus.eu>). Some figures were generated using Generic Mapping Tools software (Wessel et al., 2013). This work was supported by a Chinese Scholarship Council-University of Leeds joint scholarship awarded to Lin Shen. This work was also supported by the Centre for the Observation and Modelling of Earthquakes, Volcanoes and Tectonics (COMET) in the United Kingdom. John Elliott acknowledges support from the Royal Society through a University Research Fellowship (UF150282). This work was supported by NERC through the Looking into the Continents from Space (LiCS) large grant (NE/K010867/1).

- Dee, D. P., Uppala, S., Simmons, A., Berrisford, P., Poli, P., Kobayashi, S., et al. (2011). The ERA-Interim reanalysis: Configuration and performance of the data assimilation system. *Quarterly Journal of the Royal Meteorological Society*, *137*(656), 553–597.
- Delacourt, C., Briole, P., & Achache, J. (1998). Tropospheric corrections of SAR interferograms with strong topography, Application to Etna. *Geophysical Research Letters*, *25*(15), 2849–2852.
- Delouis, B., Nocquet, J.-M., & Vallée, M. (2010). Slip distribution of the February 27, 2010 $M_w = 8.8$ Maule earthquake, central Chile, from static and high-rate GPS, InSAR, and broadband teleseismic data. *Geophysical Research Letters*, *37*, L17305. <https://doi.org/10.1029/2010GL043899>
- Doin, M.-P., Lasserre, C., Peltzer, G., Cavalié, O., & Doubre, C. (2009). Corrections of stratified tropospheric delays in SAR interferometry: Validation with global atmospheric models. *Journal of Applied Geophysics*, *69*(1), 35–50.
- Efron, B., & Tibshirani, R. J. (1994). *An introduction to the bootstrap*. Boca Raton: CRC Press.
- Elliott, J. R., Biggs, J., Parsons, B., & Wright, T. (2008). InSAR slip rate determination on the Altyn Tagh Fault, northern Tibet, in the presence of topographically correlated atmospheric delays. *Geophysical Research Letters*, *35*, L12309. <https://doi.org/10.1029/2008GL033659>
- Elliott, J. R., Walters, R., & Wright, T. (2016). The role of space-based observation in understanding and responding to active tectonics and earthquakes. *Nature Communications*, *7*, 13844.
- Farr, T. G., Rosen, P. A., Caro, E., Crippen, R., Duren, R., Hensley, S., et al. (2007). The shuttle radar topography mission. *Reviews of Geophysics*, *45*, RG2004. <https://doi.org/10.1029/2005RG000183>
- Fialko, Y. (2006). Interseismic strain accumulation and the earthquake potential on the southern San Andreas fault system. *Nature*, *441*(7096), 968–971.
- Foster, J., Kealy, J., Cherubini, T., Businger, S., Lu, Z., & Murphy, M. (2013). The utility of atmospheric analyses for the mitigation of artifacts in InSAR. *Journal of Geophysical Research: Solid Earth*, *118*, 748–758. <https://doi.org/10.1002/jgrb.50093>
- Fournier, T., Pritchard, M. E., & Finnegan, N. (2011). Accounting for atmospheric delays in InSAR data in a search for long-wavelength deformation in South America. *IEEE Transactions on Geoscience and Remote Sensing*, *49*(10), 3856–3867.
- Funning, G. J., Parsons, B., & Wright, T. J. (2007). Fault slip in the 1997 Manyi, Tibet earthquake from linear elastic modelling of InSAR displacements. *Geophysical Journal International*, *169*(3), 988–1008.
- Gong, W., Meyer, F. J., Liu, S., & Hanssen, R. F. (2015). Temporal filtering of InSAR data using statistical parameters from NWP models. *IEEE Transactions on Geoscience and Remote Sensing*, *53*(7), 4033–4044.
- Hamling, I. J., Hreinsdóttir, S., Clark, K., Elliott, J. R., Liang, C., Fielding, E., et al. (2017). Complex multifault rupture during the 2016 Mw 7.8 Kaikōura earthquake, New Zealand. *Science*, *356*(6334), eaam7194.
- Hanssen, R. F. (2001). *Radar interferometry: Data interpretation and error analysis* (Vol. 2). New York: Springer Science & Business Media.
- He, J., Lu, S., & Wang, W. (2013). Three-dimensional mechanical modeling of the GPS velocity field around the northeastern Tibetan plateau and surrounding regions. *Tectonophysics*, *584*, 257–266.
- He, J., Vernant, P., Chéry, J., Wang, W., Lu, S., Ku, W., et al. (2013). Nailing down the slip rate of the Altyn Tagh Fault. *Geophysical Research Letters*, *40*, 5382–5386. <https://doi.org/10.1002/2013GL057497>
- Heleno, S. I., Frischknecht, C., d'Oreye, N., Lima, J., Faria, B., Wall, R., & Kervyn, F. (2010). Seasonal tropospheric influence on SAR interferograms near the ITCZ—The case of Fogo Volcano and Mount Cameroon. *Journal of African Earth Sciences*, *58*(5), 833–856.
- Herring, T., King, R., & McClusky, S. (2015). Introduction to GAMIT/GLOBK, release 10.6. Massachusetts Institute of Technology, 2015.
- Hooper, A. (2008). A multi-temporal InSAR method incorporating both persistent scatterer and small baseline approaches. *Geophysical Research Letters*, *35*, L16302. <https://doi.org/10.1029/2008GL034654>
- Hooper, A. (2010). A statistical-cost approach to unwrapping the phase of InSAR time series. In *Proc. Fringe 2009 Workshop* (pp. 1–6).
- Hooper, A., Bekaert, D., Spaans, K., & Arkan, M. (2012). Recent advances in SAR interferometry time series analysis for measuring crustal deformation. *Tectonophysics*, *514*, 1–13.
- Hussain, E., Hooper, A., Wright, T. J., Walters, R. J., & Bekaert, D. P. (2016). Interseismic strain accumulation across the central North Anatolian Fault from iteratively unwrapped InSAR measurements. *Journal of Geophysical Research: Solid Earth*, *121*, 9000–9019. <https://doi.org/10.1002/2016JB013108>
- Jolivet, R., Agram, P. S., Lin, N. Y., Simons, M., Doin, M.-P., Peltzer, G., & Li, Z. (2014). Improving InSAR geodesy using global atmospheric models. *Journal of Geophysical Research: Solid Earth*, *119*, 2324–2341. <https://doi.org/10.1002/2013JB010588>
- Jolivet, R., Cattin, R., Chamot-Rooke, N., Lasserre, C., & Peltzer, G. (2008). Thin-plate modeling of interseismic deformation and asymmetry across the Altyn Tagh Fault zone. *Geophysical Research Letters*, *35*, L02309. <https://doi.org/10.1029/2007GL031511>
- Li, Z., Fielding, E. J., Cross, P., & Muller, J.-P. (2006). Interferometric synthetic aperture radar atmospheric correction: GPS topography-dependent turbulence model. *Journal of Geophysical Research*, *111*, B02404. <https://doi.org/10.1029/2005JB003711>
- Li, Z., Fielding, E., Cross, P., & Preusker, R. (2009). Advanced InSAR atmospheric correction: MERIS/MODIS combination and stacked water vapour models. *International Journal of Remote Sensing*, *30*(13), 3343–3363.
- Liang, S., Gan, W., Shen, C., Xiao, G., Liu, J., Chen, W., et al. (2013). Three-dimensional velocity field of present-day crustal motion of the Tibetan Plateau derived from GPS measurements. *Journal of Geophysical Research: Solid Earth*, *118*, 5722–5732. <https://doi.org/10.1002/2013JB010503>
- Lin, Y. N., Simons, M., Hetland, E. A., Muse, P., & DiCaprio, C. (2010). A multiscale approach to estimating topographically correlated propagation delays in radar interferograms. *Geochemistry, Geophysics, Geosystems*, *11*, Q09002. <https://doi.org/10.1029/2010GC003228>
- Lindsey, E. O., Natsuaki, R., Xu, X., Shimada, M., Hashimoto, M., Melgar, D., & Sandwell, D. T. (2015). Line-of-sight displacement from ALOS-2 interferometry: M_w 7.8 Gorkha Earthquake and M_w 7.3 aftershock. *Geophysical Research Letters*, *42*, 6655–6661. <https://doi.org/10.1002/2015GL065385>
- Onn, F., & Zebker, H. (2006). Correction for interferometric synthetic aperture radar atmospheric phase artifacts using time series of zenith wet delay observations from a GPS network. *Journal of Geophysical Research*, *111*, B09102. <https://doi.org/10.1029/2005JB004012>
- Parker, A. L., Biggs, J., Walters, R. J., Ebmeier, S. K., & Wright, T. J. (2015). Systematic assessment of atmospheric uncertainties for InSAR data at volcanic arcs using large-scale atmospheric models: Application to the Cascade volcanoes, United States. *Remote Sensing of Environment*, *170*, 102–114.
- Perissin, D., & Wang, T. (2011). Time-series InSAR applications over urban areas in China. *IEEE Journal of Selected Topics in Applied Earth Observations and Remote Sensing*, *4*(1), 92–100.
- Pinel, V., Hooper, A., De la Cruz-Reyna, S., Reyes-Davila, G., Doin, M., & Bascou, P. (2011). The challenging retrieval of the displacement field from InSAR data for andesitic stratovolcanoes: Case study of Popocatepetl and Colima Volcano, Mexico. *Journal of Volcanology and Geothermal Research*, *200*(1), 49–61.
- Puntanen, S., Styan, G. P., & Werner, H. J. (2000). Two matrix-based proofs that the linear estimator Gy is the best linear unbiased estimator. *Journal of Statistical Planning and Inference*, *88*(2), 173–179.

- Puységur, B., Michel, R., & Avouac, J.-P. (2007). Tropospheric phase delay in interferometric synthetic aperture radar estimated from meteorological model and multispectral imagery. *Journal of Geophysical Research*, *112*, B05419. <https://doi.org/10.1029/2006JB004352>
- Ryder, I., Parsons, B., Wright, T. J., & Funning, G. J. (2007). Post-seismic motion following the 1997 Manyi (Tibet) earthquake: InSAR observations and modelling. *Geophysical Journal International*, *169*(3), 1009–1027.
- Savage, J., & Burford, R. (1973). Geodetic determination of relative plate motion in central California. *Journal of Geophysical Research*, *78*(5), 832–845.
- Searle, M. P., Elliott, J., Phillips, R., & Chung, S.-L. (2011). Crustal-lithospheric structure and continental extrusion of Tibet. *Journal of the Geological Society*, *168*(3), 633–672.
- Sigmundsson, F., Hooper, A., Hreinsdóttir, S., Vogfjörð, K. S., Ófeigsson, B. G., Heimisson, E. R., et al. (2015). Segmented lateral dyke growth in a rifting event at Bárðarbunga volcanic system, Iceland. *Nature*, *517*(7533), 191–195.
- Singleton, A., Li, Z., Hoey, T., & Muller, J.-P. (2014). Evaluating sub-pixel offset techniques as an alternative to D-InSAR for monitoring episodic landslide movements in vegetated terrain. *Remote Sensing of Environment*, *147*, 133–144.
- Smith, E. K., & Weintraub, S. (1953). The constants in the equation for atmospheric refractive index at radio frequencies. *Proceedings of the IRE*, *41*(8), 1035–1037.
- Tapponnier, P., Zhiqin, X., Roger, F., Meyer, B., Arnaud, N., Wittlinger, G., & Jingsui, Y. (2001). Oblique stepwise rise and growth of the Tibet Plateau. *Science*, *294*(5547), 1671–1677.
- Taylor, M., & Peltzer, G. (2006). Current slip rates on conjugate strike-slip faults in central Tibet using synthetic aperture radar interferometry. *Journal of Geophysical Research*, *111*, B12402. <https://doi.org/10.1029/2005JB004014>
- Walters, R., Elliott, J. R., Li, Z., & Parsons, B. (2013). Rapid strain accumulation on the Ashkabad fault (Turkmenistan) from atmosphere-corrected InSAR. *Journal of Geophysical Research: Solid Earth*, *118*, 3674–3690. <https://doi.org/10.1002/jgrb.50236>
- Wang, H., Xu, C., & Ge, L. (2007). Coseismic deformation and slip distribution of the 1997 Mw7. 5 Manyi, Tibet, earthquake from InSAR measurements. *Journal of Geodynamics*, *44*(3–5), 200–212.
- Wei, M., Sandwell, D., & Smith-Konter, B. (2010). Optimal combination of InSAR and GPS for measuring interseismic crustal deformation. *Advances in Space Research*, *46*(2), 236–249.
- Wessel, P., Smith, W. H., Scharroo, R., Luis, J., & Wobbe, F. (2013). Generic mapping tools: Improved version released. *Eos, Transactions American Geophysical Union*, *94*(45), 409–410.
- Wicks, C. W., Dzurisin, D., Ingebritsen, S., Thatcher, W., Lu, Z., & Iverson, J. (2002). Magmatic activity beneath the quiescent Three Sisters volcanic center, central Oregon Cascade Range, USA. *Geophysical Research Letters*, *29*(7), 1122. <https://doi.org/10.1029/2001GL014205>
- Wright, T., Gonzalez, P., Walters, R., Hatton, E., Spaans, K., & Hooper, A. (2016). LiCSAR: tools for automated generation of Sentinel-1 frame interferograms. In *AGU Fall Meeting Abstracts*, G23A–1037.
- Yin, Y., Zheng, W., Liu, Y., Zhang, J., & Li, X. (2010). Integration of GPS with InSAR to monitoring of the Jiayu landslide in Sichuan, China. *Landslides*, *7*(3), 359–365.
- Yu, C., Penna, N. T., & Li, Z. (2017). Generation of real-time mode high-resolution water vapor fields from GPS observations. *Journal of Geophysical Research: Atmospheres*, *122*, 2008–2025. <https://doi.org/10.1002/2016JD025753>
- Yun, Y., Zeng, Q., Green, B. W., & Zhang, F. (2015). Mitigating atmospheric effects in InSAR measurements through high-resolution data assimilation and numerical simulations with a weather prediction model. *International Journal of Remote Sensing*, *36*(8), 2129–2147.
- Zebker, H. A., Rosen, P. A., & Hensley, S. (1997). Atmospheric effects in interferometric synthetic aperture radar surface deformation and topographic maps. *Journal of Geophysical Research*, *102*(B4), 7547–7563.

Erratum

The originally published version of this article omitted from the Acknowledgments that the work was supported by NERC through the Looking into the Continents from Space (LiCS) large grant (NE/K010867/1). This has been corrected, and this may be considered the official version of record.